2D modelling of polycrystalline silicon thin film solar cells

Ana-Maria Teodoreanu[1,a], Felice Friedrich[1], Rainer Leihkauf[1], Christian Boit[1], Caspar Leendertz[2], and Lars Korte[2]

[1] Technische Universität Berlin, Semiconductor Devices Division, PVcomB, Einsteinufer 19, Sekr. E2, 10587 Berlin, Germany
[2] Helmholtz-Zentrum Berlin, Institute for Silicon Photovoltaics, Kekuléstrasse 5, 12489 Berlin, Germany

Abstract The influence of grain boundary (GB) properties on device parameters of polycrystalline silicon (poly-Si) thin film solar cells is investigated by two-dimensional device simulation. A realistic poly-Si thin film model cell composed of antireflection layer, (n^+)-type emitter, 1.5 μm thick p-type absorber, and (p^+)-type back surface field was created. The absorber consists of a low-defect crystalline Si grain with an adjacent highly defective grain boundary layer. The performances of a reference cell without GB, one with n-type and one with p-type GB, respectively, are compared. The doping concentration and defect density at the GB are varied. It is shown that the impact of the grain boundary on the poly-Si cell is twofold: a local potential barrier is created at the GB, and a part of the photogenerated current flows within the GB. Regarding the cell performance, a highly doped n-type GB is less critical in terms of the cell's short circuit current than a highly doped p-type GB, but more detrimental in terms of the cell's open circuit voltage and fill factor.

1 Introduction

Polycrystalline silicon (poly-Si) is an attractive absorber material for thin film solar cells. Ideally, the high stability against degradation of crystalline silicon can be combined with low-cost production. The reduced optical thickness of thin-film cells leading to incomplete absorption of the solar spectrum, and thus to low short circuit currents J_{SC}, can be quite successfully remedied by different light trapping approaches [1, 2]. Current research on poly-Si focuses on minimizing the critical influence of grain boundaries (GBs) as centers of recombination in the material, which act on the cell's open circuit voltage V_{OC}. Indeed, high efficiencies of 20.4% and corresponding high V_{OC}s of 664 mV were already achieved with multicrystalline silicon wafer solar cells [3]. However, the best poly-Si thin film solar cells today show significantly lower efficiencies of 10.4% [4] and record V_{OC}s of up to 582 mV [5–7], depending on the poly-Si material manufacturing method and contacting scheme. This demonstrates that there is a need but also a potential of improvement of the poly-Si material.

In contrast to their multicrystalline counterpart (i.e. wafer-based cell with diffused junction) poly-Si thin-film solar cells feature a number of layers with different functionality in very close proximity, rendering the local cell properties highly non-uniform. As the standard solar cell characterization methods like current-voltage (J-V) characteristics in the dark and under illumination yield only global properties, the results are usually interpreted in terms of an effective medium approach for the absorber. However, the application of this approximation is not always appropriate and relevant information can be gained by separating the material properties of grain and grain boundary. A straightforward way to investigate the individual effect of grain boundaries on the solar cell performance (e.g. on J-V characteristics) is device simulation. A number of studies on the influence of grain boundaries in silicon-based devices can be found in references [8–13]. In general, the GB is modeled as an interface layer with a specific trap density and interface recombination velocity. The literature results show that the cell efficiency deteriorates, especially when the GB is horizontal and/or located in the space charge region (SCR) [10]. However, an accumulation of impurities or dopant atoms as well as charge carrier transport within the GB, as observed experimentally in reference [14], cannot be adequately investigated with this approach.

In the present study, poly-Si thin film solar cells are investigated by 2D modelling and simulations with the numerical device simulator Sentaurus TCAD [15]. A basic 2D model of the poly-Si thin film solar cell was developed consisting of a low-defect crystalline grain and a highly defective grain boundary layer. The performance of poly-Si
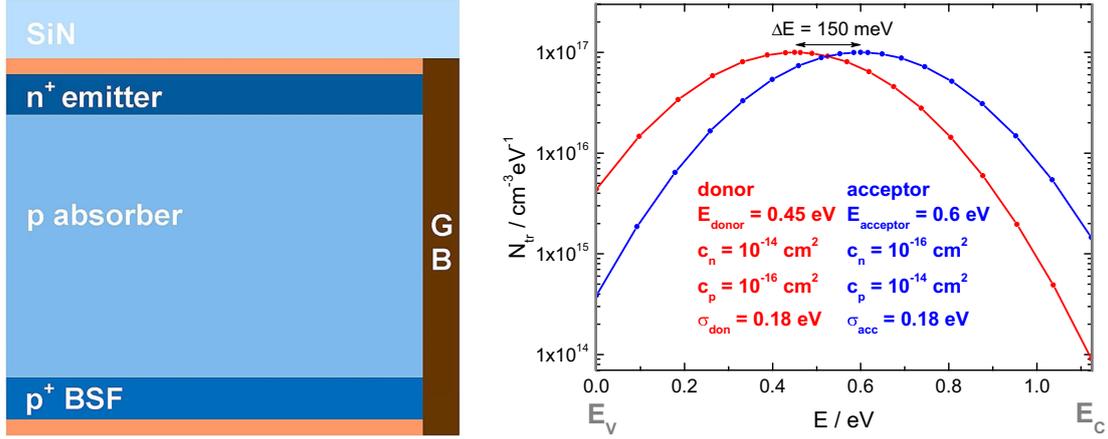
---
[a] e-mail: ana-maria.teodoreanu@tu-berlin.de

Fig. 1. Left: Structural model of the poly-Si solar cell unit composed of a p-type crystalline Si absorber grain ($2~\mu$m width), p^+ back surface field and n^+ emitter with an adjacent vertical grain boundary layer (5 nm width). The contacts, defined as ohmic, are depicted in orange. The silicon nitride (SiN) top layer represents the antireflection coating. Right: Assumed defect distribution in the GB layer over the energy in the band gap for the particular case of a GB defect density of $10^{17}~\mathrm{cm}^{-3}\,\mathrm{eV}^{-1}$. For details see Tables 1 and 2.

Table 1. Parameters of the cell's layers: emitter, absorber, BSF and GB.

	Emitter	Absorber	BSF	GB
type	n^+	p	p^+	variable
doping density/cm^{-3}	1.2×10^{20}	1.5×10^{16}	1.5×10^{19}	variable
defect density/cm^{-3}	10^{19}	10^{10}	10^{19}	variable
thickness	35 nm	1.5 μm	65 nm	1.6 μm
width	2 μm	2 μm	2 μm	5 nm

solar cells with an n-type and a p-type grain boundary, respectively, is compared to the performance of a reference cell without grain boundary. The variation in GB doping type is intended to reflect segregation of doping atoms or impurities at the GB or emitter diffusion through the GB. Within our study, only two parameters of the GB layer are varied: the doping concentration and the defect density. While the influence of the GB doping type is ambivalent dependent on the parameter range, the cell's V_{OC} in general deteriorates in the presence of a GB.

2 Modelling approach

For the implementation of non-horizontal (in the present case vertical) GBs in an optoelectronic solar cell model it is essential to use a 2D/3D numerical device simulator. The results presented in this study were obtained with Sentaurus TCAD from Synopsys [15]. Basic silicon parameters were taken from AFORS-HET [16]. For the optical modelling, we used the transfer matrix method (TMM) implemented in Sentaurus TCAD [17]. The simulations were performed at standard testing conditions (AM1.5 global spectrum, 100 mW/cm^2 radiant power density and 25 °C operating temperature).

The basic structure of the simulated poly-Si thin-film solar cells is shown in Figure 1 together with the assumed defect distribution in the GB over the energy in the band gap. Table 1 lists the parameters of the solar cell layers.

The poly-Si growth is assumed to be columnar with a lateral Si grain size of 2 μm and a film thickness of 1.6 μm. The vertical grain boundary is assumed to be 5 nm wide, which is in agreement with experimental observations [18]. In addition to the p-type absorber an n^+ emitter as well as a p^+ back surface field (BSF) were considered. The adjacent electrical contacts are assumed to be ohmic and transparent and at boundaries of the device that are not contacts Neumann boundary conditions were applied. Finally, a 100 nm thick SiN layer was implemented as antireflection coating for the optical TMM calculation of the generation rate.

The absorber grain is p-type crystalline silicon (c-Si) doped $1.5 \times 10^{16}~\mathrm{cm}^{-3}$ and having a typical low defect concentration of $10^{10}~\mathrm{cm}^{-3}$ with capture cross sections for electrons and holes of $10^{-14}~\mathrm{cm}^2$, represented by a single defect in the middle of the band gap. The emitter and BSF layers are highly doped with $1.2 \times 10^{20}~\mathrm{cm}^{-3}$ and $1.5 \times 10^{19}~\mathrm{cm}^{-3}$, respectively, and have a single defect of $10^{19}~\mathrm{cm}^{-3}$ concentration in the middle of the bandgap, with capture cross sections for electrons and holes of $10^{-14}~\mathrm{cm}^2$. The band gap, the mobilities for electrons and holes, and the densities of states of the valence and conduction bands are standard doping-dependent parameters of c-Si [19].

The GB layer is modeled as a highly defective silicon layer with a continuous dangling bond-like density of states distribution in the band gap (cf. Fig. 1, right) [20]. The electronic properties and defect specifications for the

Table 2. Parameters of the GB layer. For the density of states in the band gap are specified: the energetic position of the maximum defect densities for the donor-type and the acceptor-type defect distribution $E_{\text{donor, acceptor}}$, the maximum defect density of the distributions N_{tr}, the capture cross sections for electrons and holes $c_{\text{n,p}}$ and the standard deviation σ.

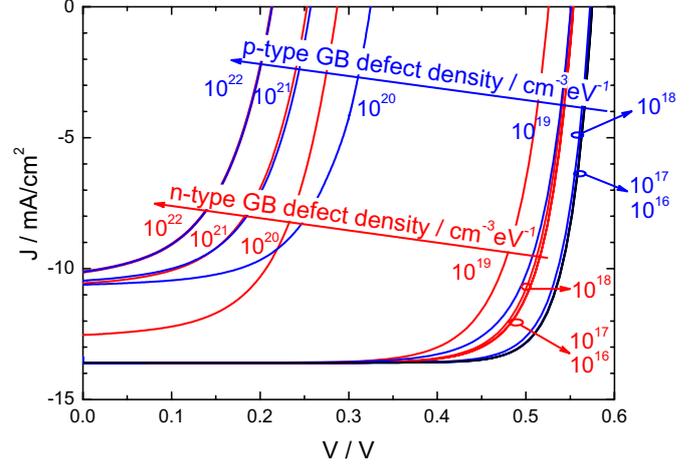| Layer properties		
bandgap, E_{G}	1.059 eV	
density of states		
of the conduction band,	8.020×10^{18} cm^{-3}	
N_{C} density of states		
of the valence band, N_{V}	7.566×10^{18} cm^{-3}	
electron mobility, μ_{n}	193.60 cm^2/V s	
hole mobility, μ_{p}	68.93 cm^2/V s	
Density of states in the band gap		
defect type	donor	acceptor
$E_{\text{donor, acceptor}}$	0.40 eV	0.65 eV
N_{tr}	10^{16}–10^{22} cm^{-3} eV^{-1}	
c_{n}	10^{-14} cm^2	10^{-16} cm^2
c_{p}	10^{-16} cm^2	10^{-14} cm^2
σ	0.18 eV	

Fig. 2. Calculated J-V characteristics under illumination of the structures A (black line), B (blue lines) and C (red lines) for a highly doped GB with $N_{\text{A,D}} = 10^{19}$ cm^{-3} at varying GB defect densities.

GB layer are summarized in Table 2. For this layer the doping type (p or n), the doping density N_{A} or N_{D}, respectively, and the defect density N_{tr} (corresponding to the maximum defect density of the Gaussian distribution in Fig. 1) were varied, the former ranging from 10^{15}–10^{20} cm^{-3} and the latter from 10^{16}–10^{22} cm^{-3} eV^{-1}. All other parameters such as the band gap, density of states of the valence and conduction band, and mobilities were kept constant. The values are based on reference [19] for heavily doped c-Si with $N_{\text{A}} = 1.5 \times 10^{19}$ cm^{-3}. The dangling bond-like defects are represented by two Gaussian distributions within the band gap, shifted relative to each other by the correlation energy ΔE, which was determined to be in the range of 100 meV to 200 meV [20]. We chose for our simulations an average $\Delta E = 150$ meV.

In the following, the reference cell without GB layer will be denoted A, the cell with p-type GB layer B and the cell with n-type GB layer C.

3 Simulation results

Current-voltage characteristics under illumination were calculated for the reference cell A (without GB) as well as cell B (with p-type GB) and cell C (with n-type GB) for varying GB doping concentration $N_{\text{A,D}}$ and GB defect concentration N_{tr}.

Figure 2 shows the J-V characteristics for a highly doped GB layer with $N_{\text{A,D}} = 10^{19}$ cm^{-3} and varying N_{tr}. The highest V_{OC} is observed for the reference cell as well as cell B in the low GB defect range of 10^{16} and 10^{17} cm^{-3} eV^{-1}. A deterioration of the J_{SC} is generally not observed until the GB defect density exceeds 10^{19} cm^{-3} eV^{-1}. For higher defect densities in the GB of 10^{21} and 10^{22} cm^{-3} eV^{-1}, the cell's V_{OC} as well as J_{SC} are significantly reduced for both cell structures B and C in an equal way. A remarkable difference of the solar cell

characteristics between the structure B and C is found at the intermediate GB defect density of 10^{20} cm^{-3} eV^{-1}: we observe higher J_{SC} for cell C and higher V_{OC} for cell B.

The solar cell parameters J_{SC}, V_{OC}, fill factor FF and efficiency η extracted from the illuminated J-V curves are shown in Figure 3 for the whole range of GB doping concentration $N_{\text{A,D}}$ and GB defect density N_{tr}. For better comparability, the solar cell parameters of the cells B and C were normalized to the values calculated for reference cell A.

We can distinguish three regimes: **(1)** the high defect density regime $N_{\text{tr}} \gg N_{\text{A,D}}$, **(2)** the low defect density regime $N_{\text{tr}} \ll N_{\text{A,D}}$ and **(3)** the intermediate regime, where the GB defect density is in the range of GB doping density.

For defect densities higher than the doping level **(1)**, corresponding to the lower left corner of Figure 3, the solar cell performance is almost independent on the doping level or type. An increased defect density in the GB leads to an overall decrease of the solar cell efficiency of up to 84%. Most affected is the cell's V_{OC} with up to 64% followed by the FF with up to 39% and the J_{SC} with up to 26%.

The regime **(2)** of $N_{\text{tr}} \ll N_{\text{A,D}}$, corresponding to the upper right corner in Figure 3, is defined by equal J_{SC} values for cell types B and cell C, that are also close to the reference cell value. In contrast, V_{OC}, FF and η are higher for cell B.

In the intermediate regime **(3)** the J_{SC} of cell C is higher than that of cell B whereas the V_{OC}, FF and η of cell B are higher than those of cell C.

4 Discussion

The interplay between GB doping concentration and GB defect density determines the Fermi level in the GB layer, which is in general different from the Fermi level
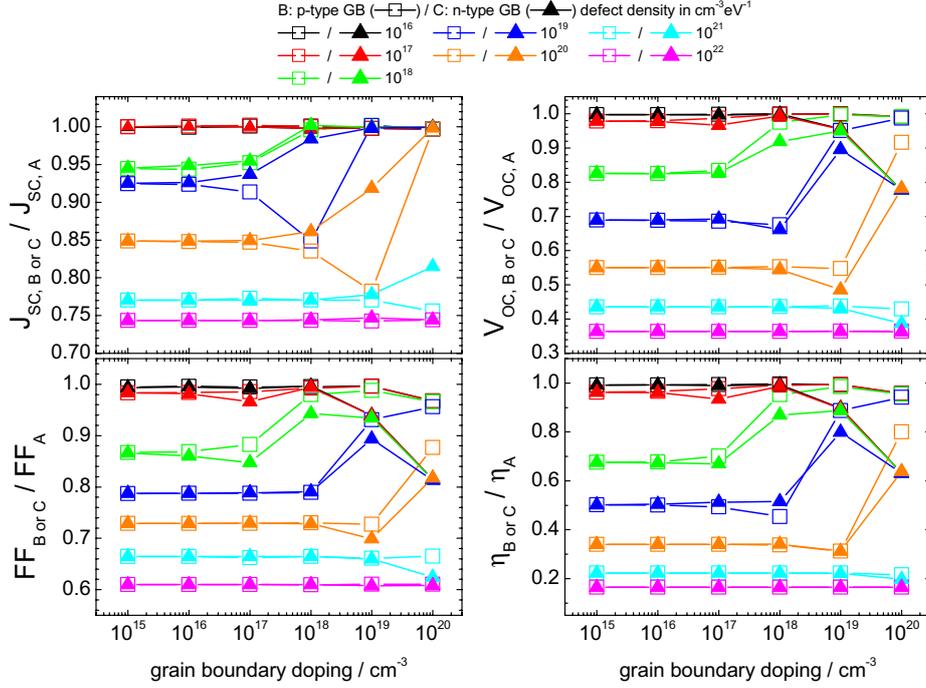
Fig. 3. Simulations of the solar cell parameters of the structure B (with *p*-type GB) and C (with *n*-type GB) normalized to the corresponding solar cell parameters of structure A (without any GB, reference cell) $J_{SC,B\ or\ C}/J_{SC,A}$, $V_{OC,B\ or\ C}/V_{OC,A}$, $FF_{B\ or\ C}/FF_A$ and $\eta_{B\ or\ C}/\eta_A$ for varying GB doping concentration (abscissae) and for different GB defect densities (symbol slopes).
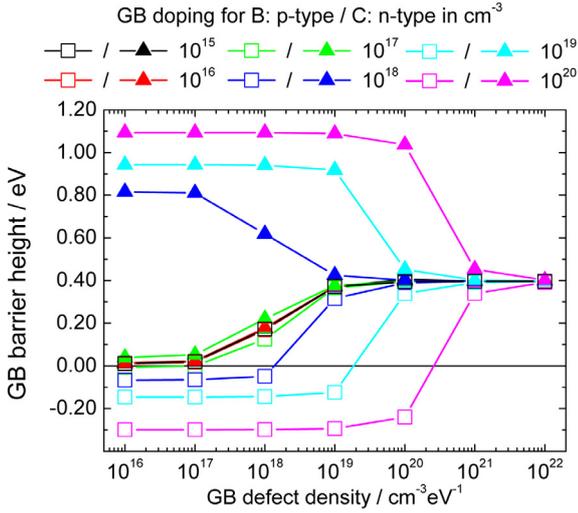

Fig. 4. Calculated potential barrier height at the interface grain-GB, in the bulk of the solar cell. The results are shown over the GB defect density (abscissae) for different GB doping concentrations (symbol slopes) and for the structures B and C.

inside the grain. Thus, a potential barrier forms in the structure at the interface grain-GB. The height of this barrier relative to the conduction band maximum was calculated for a position in the field-free bulk far from the BSF and emitter. Figure 4 shows the potential barrier height over the GB defect density for the specified doping range for cells B and C.

If we consider the three regimes defined above: the regime **(1)** of higher defect density $N_{tr} \gg N_{A,D}$ is governed by a Fermi level pinning effect, leading to a potential barrier height of ~ 0.4 eV, which is independent of doping. This explains the similarity of the *J-V* characteristics for cases B and C in this regime in Figure 2 and of the GB doping-independent solar cell parameters at high N_{tr} in Figure 3. This corresponds to the case of for example a non-passivated poly-Si absorber.

Only in regime **(2)** for $N_{tr} \ll N_{A,D}$, the barrier height is determined by the respective doping, leading to a negative potential barrier for *p*-type GB and a pronounced positive potential barrier in the cell with *n*-type GB. Due to these potential barriers, the *p*-type GB layer acts electron-repulsive – like an additional "back surface field" and the *n*-type GB acts hole repulsive – forming an additional *pn* junction at the interface grain-GB.

Figure 5 shows the electron and hole current densities for the three structures at short circuit conditions in the case of $N_{A,D} = 10^{20}$ cm^{-3} and $N_{tr} = 10^{16}$ cm^{-3} eV^{-1}. Indeed, for *p*-type doping, the simulation shows a local quenching of the space charge region (SCR) in the vicinity of the GB, and for *n*-type doping an extension of the *pn* junction along the GB. However, the additional *pn* junction which forms at the interface grain-GB proves to be detrimental for the cell efficiency, which decreases by over 30% mainly due to the decrease in V_{OC}. In literature, beneficial effects of extended *pn* junctions are discussed [21]. We also observe such effects in the intermediate regime **(3)**. Here, a larger J_{SC} is determined for the *n*-type GB in cell C compared to cell B. However, the V_{OC}
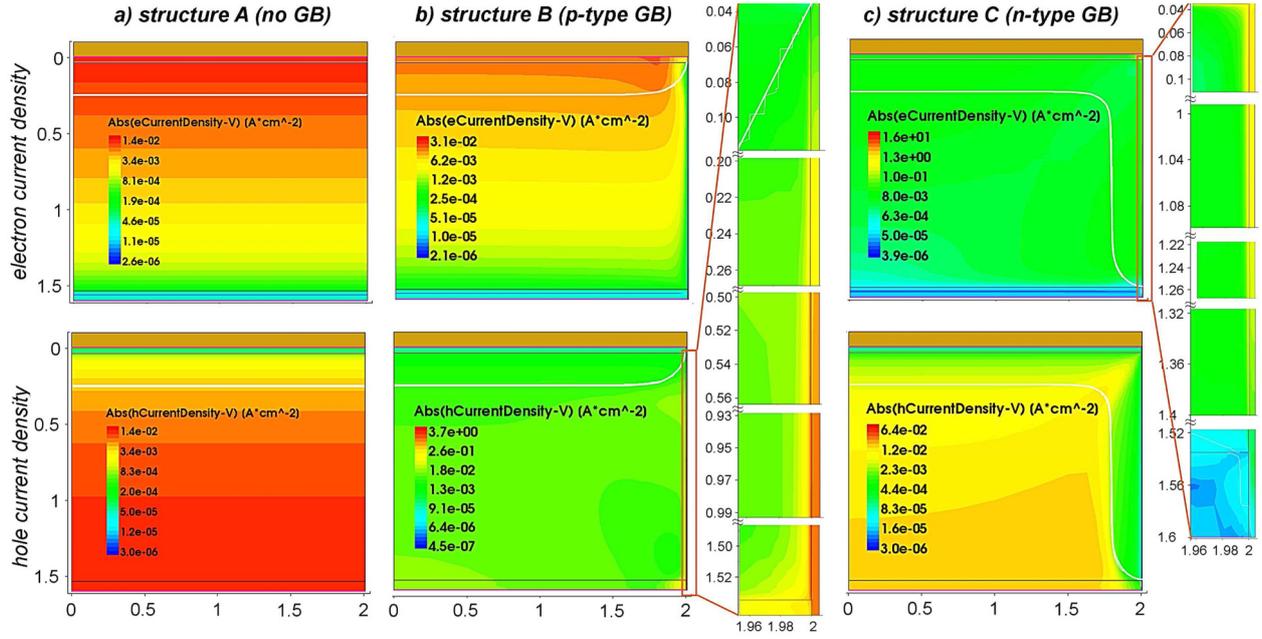
Fig. 5. Exemplary 2D simulations of the electron and hole current density distributions in the cell at short circuit conditions for (a) structure A, (b) structure B and (c) structure C. The GB doping concentration is 10^{20} cm^{-3} and the GB defect density 10^{16} cm^{-3} eV^{-1}. The boundary of the space charge region is marked with a white line. The zoom-in into the GB layer shows the extremely high majority-carrier current in the GB increasing towards the respective majority carrier contacts.

and FF of the p-type GB cell exceed those of the n-type GB cell.

Further, for the higher doping regime **(2)**, the simulation results in Figures 5b and 5c indicate the formation of a conductive channel extending along the GB and in its vicinity, from emitter to BSF. This corresponds to the case of an enhanced emitter diffusivity within the GB or an accumulation of dopant atoms in the GB, respectively.

The respective electron and hole current densities within the GB layer are depicted in Figure 6 for the whole parameter range. For n- as well as p-type GB there is a high majority-carrier current density for GB doping concentrations of 10^{18}–10^{20} cm^{-3} (regime **(2)**). This current density is about two orders of magnitude higher than the GB current density for lower doping concentrations, forming in the high-doping regime the conductive channel. The presence of such a conductive channel is of course detrimental for the solar cell, as it effectively corresponds to a shunt of the cell. This explains the decrease in fill factor and efficiency, respectively – observed in Figure 3 in this regime. This effect is even more detrimental for a GB directly connected to the ohmic contact region (not shown here).
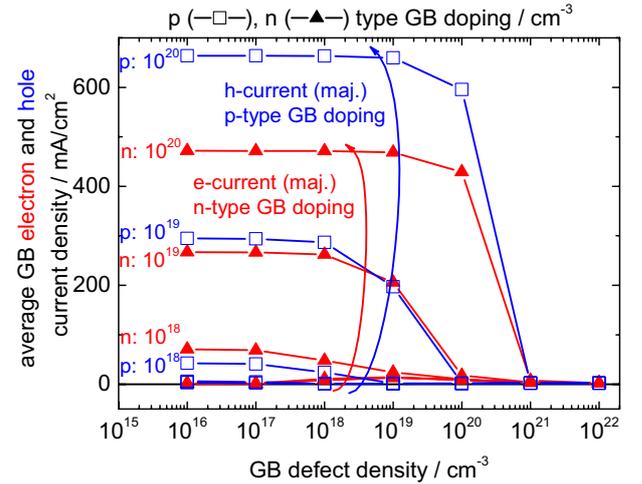

Fig. 6. Average GB electron (red symbols) and hole (blue symbols) current density shown over the GB defect density for different GB doping concentrations for p-type GB (open squares) and n-type GB (full triangles). The majority-carrier (maj.) current increase is highlighted.

5 Conclusions and outlook

The present simulation study shows, that despite the positive effects like the extension of pn junction or the formation of a BSF, that doped GB layers could bring along, both n- and p-type grain boundaries deteriorate the performance of a polycrystalline thin film solar cell. The most important factor for cell performance deterioration is the GB defect density, notably for the regime where the GB defect concentration is higher than the GB doping concentration, which features Fermi level pinning. Another important factor of the cell's characteristics is the formation conductive channel along the GB and in its vicinity, which characterizes the regime of high GB doping concentration and low GB defect density.

The simulation study can further be extended by the implementation of a transparent conductive oxide layer to refine the contacting of the grain and GB layer as well as a detailed analysis of the dark J-V characteristics.

References

1. B. Rech, H. Wagner, Appl. Phys. A: Mater. Sci. Proc. **69**, 155 (1999)
2. R. Brendel, *Thin-Film Crystalline Silicon Solar Cells*, 1st edn. (Wiley-VCH, Weinheim, 2003)
3. O. Schultz, S.W. Glunz, G.P. Willeke, Prog. Photovolt. Res. Appl. **12**, 553 (2004)
4. M.J. Keevers, T.L. Young, U. Schubert, M.A. Green, in *Proceedings of the 22nd European Photovoltaic Solar Energy Conference, 3-7 September 2007, Milan, Italy, 2007*
5. D. Amkreutz, J. Müller, M. Schmidt, T. Hänel, T.F. Schulze, Prog. Photovolt. Res. Appl. **19**, 937 (2011)
6. J. Dore et al., EPJ Photovoltaics **4**, 40301 (2012)
7. J. Haschke, L. Jogschies, D. Amkreutz, L. Korte, B. Rech, Sol. Energy Mater. Sol. Cells **115**, 7 (2013)
8. A.K. Ghosh, C. Fishman, T. Feng, J. Appl. Phys. **51**, 446 (1980)
9. J.G. Fossum, F.A. Lindholm, IEEE Trans. Electron Devices **27**, 692 (1980)
10. M.A. Green, J. Appl. Phys. **80**, 1515 (1996)
11. S.A. Edmiston, G. Heiser, A.B. Sproul, M.A. Green, J. Appl. Phys. **80**, 6783 (1996)
12. P.P. Altermatt, G. Heiser, J. Appl. Phys. **92**, 2561 (2002)
13. K.R. Taretto, Ph.D. thesis, Institut für Physikalische Elektronik-Universität Stuttgart, 2003
14. M. Kittler, M. Reiche, Adv. Eng. Mater. **11**, 249 (2009)
15. www.synopsys.com/Tools/TCAD/
16. R. Stangl, C. Leendertz, in *Physics and Technology of Amorphous-Crystalline Heterostructure Silicon Solar Cells*, edited by W.G.J.H.M. Sark, L. Korte, F. Roca, volume 0 of *Engineering Materials* (Springer, Berlin, Heidelberg, 2011), pp. 445–458
17. Sentaurus Device User Guide Version E-2010.12, December 2010, Synopsys
18. M. Klingsporn et al., private communication and presented at EMRS, Strasbourg, France, Spring 2012
19. G. Masetti, R. Severi, S. Solmi, IEEE Trans. Electron Devices **ED-30**, 764 (1983)
20. R. Schropp, M. Zeman, *Amorphous and Microcristalline Silicon Solar Cells* (Kluwer Academic Publishers, Boston, 1998), Chap. 6
21. A. Zerga, E. Christoffel, A. Slaoui, in *3rd World Conference on Photovoltaic Energy Conversion (WCPEC-3), Osaka, Japan, May 12-16 2003*, edited by K. Kurokawa, L. Kazmerski, B.M. Nelis, M. Yamaguchi, C. Wronski, W. Sinke (2003), Vol. 2, pp. 1053–1056